nature energy

Article

https://doi.org/10.1038/s41560-024-01638-z

In situ formation of liquid crystal interphase in electrolytes with soft templating effects for aqueous dual-electrode-free batteries

Received: 15 March 2024

Accepted: 6 August 2024

Published online: 20 September 2024

Check for updates

Yuqi Li[1], Xueli Zheng[1,2], Evan Z. Carlson[1], Xin Xiao[1], Xiwen Chi[1], Yi Cui[1], Louisa C. Greenburg[1], Ge Zhang[1], Elizabeth Zhang[1], Chenwei Liu[1], Yufei Yang[1], Mun Sek Kim[1], Guangxia Feng[1], Pu Zhang[1], Hance Su[1], Xun Guan[1], Jiawei Zhou[1], Yecun Wu[1], Zhichen Xue[2], Weiyu Li[1], Michal Bajdich[3] & Yi Cui[1,2,4]

Zn/MnO_2 batteries, driven by a dual deposition reaction, are a prominent avenue for achieving high energy density in aqueous systems. Introducing an initially dual-electrode-free (anode/cathode) configuration can further boost energy density to over 200 Wh kg^{-1}, but with limited cycle life due to the poor reversibility of Zn/MnO_2 deposition and stripping. Drawing inspiration from soft templating strategies in material synthesis, here we apply this approach to electrodeposition and stripping by designing an in situ formed liquid crystal interphase. This concept is achieved by incorporating just 0.1 mM of surfactant molecules into the electrolyte, which induces favourable *c*-axis orientations in depositing both hexagonal Zn and MnO_2. This enhancement subsequently increases the deposition/stripping reversibility and promotes the cycle life of the dual-electrode-free battery, achieving 80% capacity retention after ~950 cycles. This liquid crystal interphase chemistry also holds great promise for regulating deposition in other crystal systems, opening an exciting research direction for next-generation high-energy-density and long-duration energy storage based on aqueous chemistries.

Aqueous batteries, existing for over 200 years, continue to captivate strong interests owing to their safety advantages compared to conventional lithium-ion batteries[1,2]. The key to unlocking broader applications for aqueous batteries lies in enhancing their energy density and cycle life. A promising aqueous cell chemistry features the reactive pair of Zn^{2+}/Zn at the anode[3] and Mn^{2+}/MnO_2 at the cathode[4]. This eco-friendly pairing enables an operating cell voltage of approximately 2 V and a two-electron transfer reaction with high specific capacity[5,6]. To further enhance the energy density, an initial-anode/cathode-free design could be beneficial[7,8]. Initially, only implementing current collectors enhances energy density (Supplementary Table 1) by reducing weight/volume[9]. The dual-electrode-free design avoids the excessive use of Zn/MnO_2 and the complex electrode preparation process with convenient assembly and thus reduces the cost[10]. However, ensuring a prolonged cycling life for dual-electrode-less batteries becomes an essential hurdle, given the insufficient reversibility of Zn/MnO_2 deposition/stripping[11,12]. The deposited ε-phase MnO_2 exhibits low conductivity, and Mn^{3+} dissolution results in the depletion of active species. The competitive oxygen evolution reaction also speeds up water consumption. Furthermore, Zn plating faces challenges such as dendrite growth and hydrogen evolution

[1]Department of Materials Science and Engineering, Stanford University, Stanford, CA, USA. [2]Stanford Institute for Materials and Energy Sciences, SLAC National Accelerator Laboratory, Menlo Park, CA, USA. [3]SUNCAT Center for Interface Science and Catalysis, SLAC National Accelerator Laboratory, Menlo Park, CA, USA. [4]Department of Energy Science and Engineering, Stanford University, Stanford, CA, USA. e-mail: yicui@stanford.edu

https://doi.org/10.1038/s41560-024-01638-z

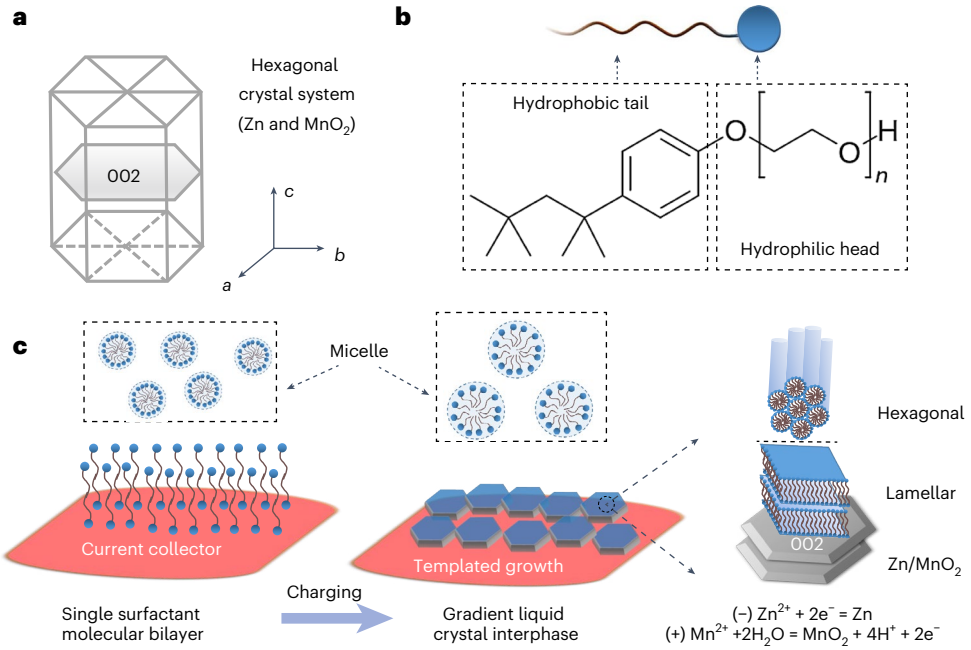

Fig. 1 | Design framework of surfactant additive for Zn/MnO_2 deposition via in situ formed liquid crystal interphase. a, Schematic illustrating the same hexagonal crystal system of Zn and (δ-/ε-) MnO_2. **b**, Molecular structure of *t*-Oct-C_6H_4-$(OCH_2CH_2)_n$OH, n = ~9–10, with typical surfactant structure including one hydrophobic tail and a hydrophilic head. **c**, Dynamic switching process from aligned surfactant molecular bilayer before deposition to gradient liquid crystal interphase including lamellar liquid crystal (close to the deposited electrode), hexagonal liquid crystal (Intermediate state) and micelle clusters (close to the electrolyte) after deposition. The reaction equations of the dual-electrode-free batteries based on Zn/MnO_2 deposition are also listed on the schematic.

reaction, which are exacerbated in full cells due to proton-induced corrosion and byproduct accumulation. Thus, adopting a cell design that is simultaneously anode-free and cathode-free is logically viable but still presents a considerable challenge.

Controlling the crystal structure of electrodeposited materials has been known to improve plating/stripping efficiency and increase cycle life. Even though both Zn and ε-MnO_2 belong to the hexagonal crystal system (Fig. 1a), no unified regulation strategy exists that could regulate the structures of both materials simultaneously in the same electrochemical cell. The success of surfactants in the soft templating methods employed in materials synthesis[13] has inspired their use as additives for conferring specific and uniform structures onto various materials[14]. Moreover, the self assembly of surfactant molecules can initiate the creation of liquid crystal templates with diverse ordered structures[15]. Although surfactant molecules are commonly employed to modify metal corrosion resistance and deposition behaviour via interfacial adsorption[16–20], liquid crystals are rarely explored in the field of batteries, typically reserved as a bulk electrolyte material to enhance ionic transport[21]. More importantly, despite these advancements, an unexplored frontier remains: liquid crystals have never been introduced as an interfacial layer (or interphase) in batteries. Employing liquid crystals as an interphase in batteries might even prove more beneficial compared with their traditional role as bulk electrolytes. Aqueous batteries often lack an inherent and effective interphase[22] and we hypothesize that in situ formation of liquid crystal interphase could afford a soft template to induce textured deposition behaviour in aqueous batteries. In addition, in situ formation of a liquid crystal interphase from a surfactant would be a low-cost and facile strategy, which can be adopted in the battery manufacturing process.

In this study, we discover a liquid crystal interphase formed in situ by the addition of a trace non-ionic surfactant (Fig. 1b). The liquid crystal interphase aligns both Zn and MnO_2 deposition along the *c* axis, substantially enhancing electrochemical cycling stability. This highly reversible dual deposition enabled the development of high-energy-density (up to 213 Wh kg^{-1}) dual-electrode-free batteries (DEFBs) with anode-free and cathode-free configurations. Soft matter characterizations revealed a dynamic switching process from an aligned surfactant molecular bilayer before deposition to a gradient liquid crystal interphase after deposition (Fig. 1c). The formation of this interphase guides templated growth of Zn and MnO_2 and explains highly reversible plating/stripping that leads to long cycle life. Specifically, Zn-MnO_2 DEFBs with 0.1 mM surfactant show the most extended cycling life with 80% capacity retention after ~950 cycles. The liquid crystal interphase surpasses traditional solid coatings by offering a flexible and dynamically adaptable interface that enhances ion transport and controls crystal orientation effectively. These properties, combined with its lower production costs and ease of application, make it particularly suitable for advancing scalable battery technology and improving the performance and longevity of electrochemical devices.

Preferential deposition orientation via surfactant additive

Deposition morphology is strongly influenced by the electrolyte choice. Balancing cost and voltage output[23], a DEFB prefers a sulfate electrolyte with 1 M $ZnSO_4$ and 1 M $MnSO_4$ formulation (denoted as the pristine electrolyte). The initial charging process will increase the concentration of proton and lower the pH value from ~4 to ~3. Whereas this enhances MnO_2 reactivity, this shift could disrupt Zn deposition[24]. To address this intricate challenge, our investigation initially focuses on the Zn side. We first examine the morphology of plated Zn. Scanning electron microscopy (SEM) images in Fig. 2a reveal a mossy, flower-like morphology on bare Cu substrate after cycling using the pristine electrolyte. These micro-flowers, ranging from 1 µm to 10 µm, consist of disordered metallic zinc sheets or zinc hydroxide sulfate (ZHS) formed through corrosion reactions[25]. These unevenly distributed corrosion products can easily lead to dendrite growth due to non-uniform electric fields.

To counteract corrosion, we developed a new aqueous 'surfactant electrolyte' by adding 0.1 mM surfactant, *t*-Oct-C_6H_4-$(OCH_2CH_2)_n$OH, n = ~9–10, into the pristine electrolyte. Surprisingly, Fig. 2b shows

https://doi.org/10.1038/s41560-024-01638-z

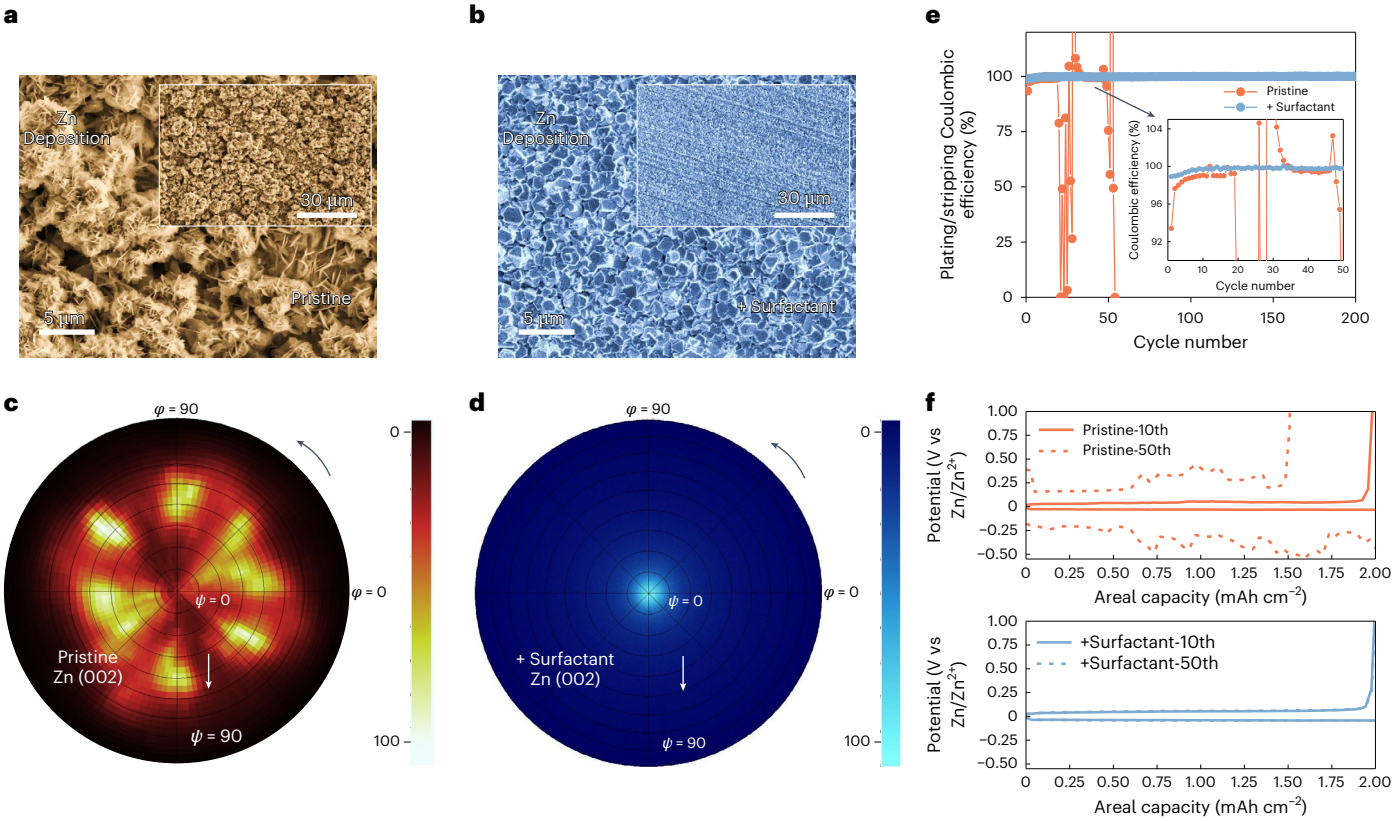

Fig. 2 | Deposition morphology and crystal structure of in situ deposited Zn metal. a,**b**, SEM images of deposited Zn using the pristine electrolyte (**a**) or surfactant electrolyte (**b**). Inset: the zoom-out SEM images. **c**,**d**, (002) Pole figure of Zn deposited in the pristine electrolyte (**c**) or surfactant electrolyte (**d**). φ is the angle of rotation that measures the azimuth of the sample in the surface plane and ψ is the tilt angle that defines the amount of tilting of the sample with respect to the normal to the sample surface. Both investigated Zn samples are disassembled from the DEFB in the fully charged state (constant voltage of 2.3 V to the charged capacity of 0.5 mAh cm^{-2}) after ten cycles. **e**, Coulombic efficiency (CE) for Zn plating/stripping as a function of cycle number of Zn/Cu cells at 2 mA and 2 mAh cm^{-2}. Inset: enlarged view of Zn plating/stripping CE in these two electrolytes. **f**, Representative charge/discharge curves of Zn/Cu cells at different cycles.

relatively uniform and small Zn flakes around 1 μm in size. These Zn flakes predominantly exhibit a hexagonal shape, corresponding to the (002) crystal face of Zn[26], which further contributes to a macroscopically flat surface topography (inset in Fig. 2b).

Additionally, X-ray diffraction (XRD) shows comparable intensities of the (002) and (100) Zn crystal planes prepared in the pristine electrolyte whereas the intensity of the (002) plane is substantially enhanced by 600% in the surfactant electrolyte (Supplementary Fig. 1). To confirm their texture, XRD (002) pole figures of Zn are measured. In Fig. 2c, the pristine electrolyte leads to a radially uneven diffraction intensity with a broad ring shape, implying a less pronounced Zn texture[27]. Conversely, using the surfactant electrolyte, the Zn (002) pole figure in Fig. 2d shows concentrated intensity at the centre, indicating a (002) out-of-plane preferred orientation of these hexagonal Zn flakes.

Zn/Cu half cells were assembled to evaluate plating/stripping reversibility. Figure 2e reveals Zn/Cu cell using the pristine electrolyte experiences fluctuating Coulombic efficiency (CE) that steeply drops after ~50 cycles. In contrast, the surfactant electrolyte maintains a high average CE over 99.9% for 200 cycles (Fig. 2e). The voltage profiles (Fig. 2f) highlight pristine electrolyte's instability and irreversible behaviour after 50 cycles. However, the surfactant electrolyte demonstrates favourable reversibility with a small voltage hysteresis, which can be attributed to the (002) plane growth, because the (002) plane promotes flat, compact Zn deposition and limits hydrogen evolution reaction activity through enhanced corrosion resistance[28].

Alignment of surfactant molecules before deposition

To understand how the surfactant facilitates Zn (002) plane emergence, we first investigate the surfactant molecule alignment on the current collector before deposition, which is pivotal for Zn atom nucleation. We immersed Cu foil in the pristine electrolyte and surfactant electrolyte (Supplementary Fig. 2). Contact angle tests (Supplementary Fig. 3) unveiled the hydrophilic nature (~48° contact angle) of pristine electrolyte-covered Cu and the super-hydrophilic nature (~0° contact angle) of surfactant electrolyte-covered Cu. This super-hydrophilic surface suggests that the outward-facing segment of the surfactant is indeed the hydrophilic head due to the hydrophobic interactions between the non-polar tails of neighbouring surfactant molecules, forming a bilayer structure as shown in Fig. 1c left[29].

To discern whether the arrangement of surfactants is organized or disordered, we designed a chemical titration experiment on the coated Cu by introducing an alkaline solution (Supplementary Fig. 4) and inferring alignment from ZHS formation. The pristine electrolyte resulted in randomly oriented ZHS sheets whereas the surfactant electrolyte produced well-ordered ZHS structures tied to the preferred (002) plane orientation[30], induced by the methodically arranged surfactant molecules. The above difference resembles the Zn morphology difference prepared in the pristine electrolyte/surfactant electrolyte, attributed to the same hexagonal system of ZHS and Zn.

Addressing the number of surfactant molecular layers, spectroscopic ellipsometry (Supplementary Fig. 5) was conducted to investigate the polarization change[31] upon reflection from the coated Cu.

https://doi.org/10.1038/s41560-024-01638-z

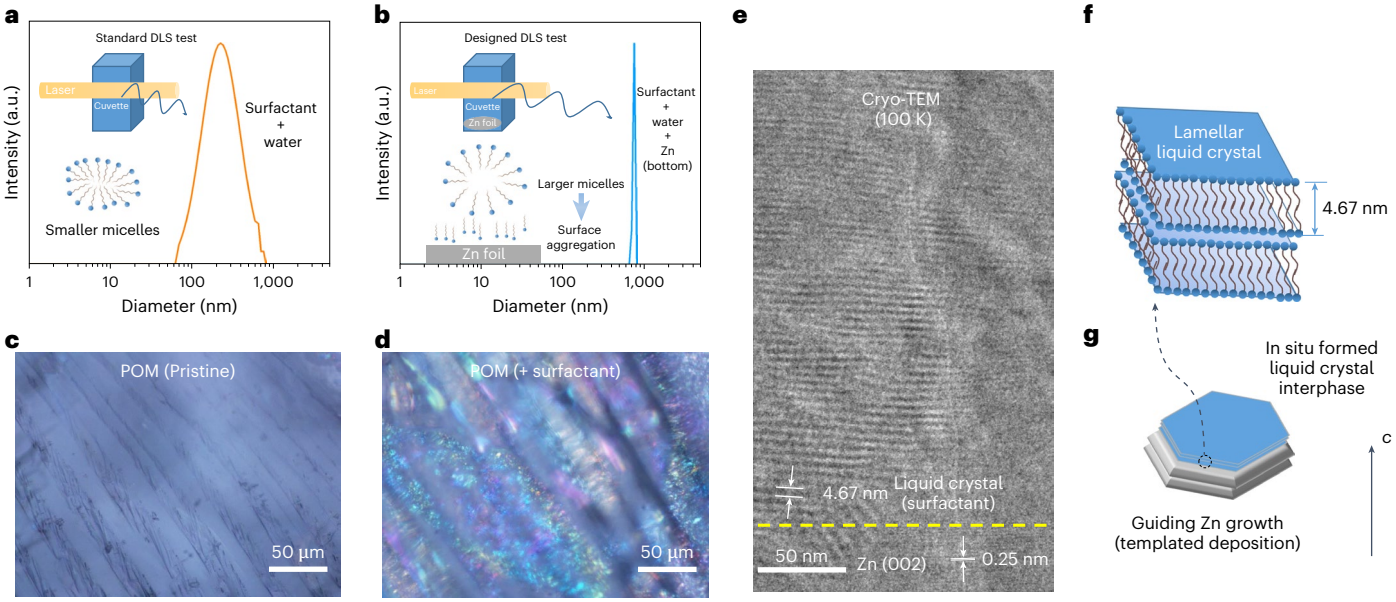

Fig. 3 | In situ formed liquid crystal interphase for templated deposition. **a**,**b**, DLS test of the surfactant aqueous solution without (**a**) and with Zn metal (**b**). Inset: schematics illustrating that the size of micelle cluster would be larger after putting the Zn metal at the bottom of cuvette considering that laser only focuses on the centre of cuvette. **c**,**d**, Polarized optical microscope image of Zn surface prepared in the pristine electrolyte (**c**) or surfactant electrolyte (**d**). **e**, High-resolution cryo-TEM image of the interface between Zn (002) and liquid crystal. The dotted lines are used to distinguish Zn (002) and liquid crystal. Note that the interface between Zn and liquid crystal is not very clear or ordered because there may be a buffer layer. **f**, Schematic illustrating the periodic structure of lamellar liquid crystal based on the Cryo-TEM results in Fig. 3e and previous literature[15,32]. The thickness of the amphiphilic bilayer in lamellar phase is ~4.67 nm. **g**, Schematic illustrating that the liquid crystal interphase can guide Zn (002) growth via templated deposition.

The measurements determine that the average thickness of the surfactant layer is approximately 5 nm, indicating a single bilayer[32]. The above experiments confirmed the aligned surfactant-bimolecular structure on Cu surface (Supplementary Fig. 6 and Fig. 1c) before deposition, which facilitates uniform Zn atom nucleation (Supplementary Fig. 7) and reduces 'dead Zn' accumulation on Cu foil (Supplementary Fig. 8) during cycling, possibly through decreased interfacial tension[33].

Liquid crystal interphase for templated deposition

Whereas the organized arrangement of surfactants in the initial state has been elucidated, the mechanism by which the surfactants guide Zn deposition with a preferred orientation remains uncertain. The key to comprehending this issue could lie in understanding the interphase between Zn and the surfactant electrolyte. We examined the interphase composition using X-ray photoelectron spectroscopy (XPS). XPS depth profiling of the Zn surface after plating in pristine electrolyte and surfactant electrolyte (Supplementary Fig. 9) reveals that the surfactant additive restricts the formation of ZHS, as evidenced by the suppressed S 2*p* spectra. Moreover, in comparison to the pristine electrolyte, XPS analysis of the Zn surface exhibited an additional peak in the O 1*s* spectra (Supplementary Fig. 10) for the surfactant electrolyte, which is ascribed to carbon–oxygen single bond, indicating the existence of organic-rich interphase due to the self-assembled surfactant. Additionally, as the etching depth increases, the intensity of the carbon–oxygen bond strengthens. This implies that the interphase structure, comprised of surfactants, thickens after deposition, possibly becoming more complex than the structure formed by a bilayer of the surfactant molecules.

Considering the interphase structure commonly extends from the electrode surface into the bulk phase of the electrolyte[34], there may be differences in the surfactant arrangement at different points in the interphase. We commence our investigation from the side closest to the bulk electrolyte. Surfactant molecules, when dissolved in water, typically form clusters known as micelles[35]. As illustrated in the inset of Fig. 3a, we utilize dynamic laser scattering (DLS) to capture the size of these micelles by focusing its laser beam at the centre of the cuvette[36]. Given that the laser does not capture signals from the bottom, we specially designed the experiment in which we place Zn metal at the bottom of the cuvette, targeting to provide an approximation of how the bulk electrolyte structure changes following zinc deposition. In comparisons between surfactant solutions with and without added Zn, the effective micelle cluster diameter was observed to increase to 745 nm (with, Fig. 3b) from 223 nm (without, Fig. 3a). We hypothesize that the self assembly of surfactant molecules at the Zn electrode interface contributes to lower surfactant concentration in the bulk phase. Dilute surfactant concentrations in water usually results in the forming of larger micelles[37].

Referring to the water–surfactant binary phase diagram[38], higher surfactant concentrations induce the formation of lyotropic liquid crystals. We utilized a polarized optical microscope (POM), a tool for studying liquid crystals and other transparent crystalline structures[39], to further characterize the interphase structure. By retaining a thin electrolyte film after disassembling cells, the Zn prepared using the pristine electrolyte exhibited no interference colours (Fig. 3c and Supplementary Fig. 11a), signifying the absence of a transparent crystal structure on its surface. In contrast, on the surfactant electrolyte sample, POM imaging shows an irregular display of radial (rainbow-like and fan-like) interference colours (Fig. 3d and Supplementary Fig. 11b). This optical pattern corresponds to the characteristics of the hexagonal phase of liquid crystals[40,41]. To further eliminate the influence of inherent colours under the POM, we focused on a specific zinc particle with a preferred orientation of (002) plane. By keeping the sample stationary and rotating the POM stage, we observed the interference colour disappearing and reappearing (Supplementary Fig. 12). This phenomenon, known as extinction[42], is a characteristic of liquid crystalline structures. It is worth noting that the interference colour of a single (002) surface remains consistent, providing evidence of a uniform orientation of the hexagonal phase on the surface[43]. On the basis of these observations, we conclude that a hexagonal liquid crystal interphase exists on the surface of the electrode.

Given that surfactants are organic components sensitive to electron beams, we employ cryogenic transmission electron microscopy

(cryo-TEM) for exploring the electrode-adjacent interphase. To study the interphase between Zn (002) and the surfactant electrolyte, we conducted Zn deposition on a Cu grid mesh assembled in a DEFB using the surfactant electrolyte. The highly porous mesh can induce Zn sheets to deposit into the pores (Supplementary Fig. 13), creating cross sections with various orientations, which facilitates our observation of the Zn/surfactant electrolyte interface. In Fig. 3e, we successfully captured the interface between Zn (002) and the surfactant electrolyte. The image reveals the lower portion consisting of Zn (002), characterized by thin lattice fringes. In stark contrast, the upper thicker layer represents the interphase, displaying a substantial layer spacing of 4.67 nm. When we compare our findings with previous research[32], we observe a striking resemblance to a lamellar phase of liquid crystal (Fig. 3f), notably due to the similarity in layer spacing. As a soft template, we believe that the lamellar liquid crystal packing on the surface of Zn (002) can guide its textured growth (Fig. 3g). The probable mechanism behind this templated deposition involves the layer-by-layer-type induction of Zn growth by the lamellar liquid crystal, elucidating our observation of an interphase with a thickness approaching ~400 nm. Some of the observed lamellar liquid crystal phases might stem from the hexagonal phase transition at lower temperatures. However, due to the operational limitations of cryo-TEM, accurately discerning the boundary between the hexagonal and lamellar phases poses challenges.

To gain atomic-level insights into the interfaces closer to the electrode, we conducted density functional theory (DFT) simulations of Zn-surfactant and Zn-H_2O interactions. We found that the most stable configuration of the surfactant molecule is the hydrophilic end vertically bonded to the Zn (002) surface (Supplementary Fig. 14). This suggests that surfactant molecules in close proximity to the Zn surface are more likely to adopt a lamellar phase arrangement rather than a hexagonal phase (relatively parallel state)[15]. Compared to the (100) and (101) planes, the adsorption is stronger between the (002) plane and the surfactant molecule (Supplementary Fig. 14), indicating that surfactant molecules can easily adsorb on Zn (002), promoting the surfactant aggregation and formation of the liquid crystal interphase, thus leading to the enlargement of textured Zn (002) during cycling. The preferred bonding interaction may help to stabilize the deposition structure, even if the lattice parameters between Zn and liquid crystal may be not perfectly matched (similar to van der Waals epitaxy)[44,45]. In contrast, water only forms weakly bound overlayers on Zn (002) (Supplementary Fig. 15). Adsorption of surfactant molecules is strongly preferred over water molecules (Supplementary Fig. 15), causing a local water-poor region near to the electrode. Thus, it is evident that we verified an in situ formed gradient liquid crystal interphase structure (micelle–hexagonal–lamellar) in Supplementary Fig. 16 and Fig. 1c, which is closely linked to the local concentration gradient of the surfactant, acting as the driving force behind liquid crystal formation. The detailed liquid crystal growth mechanism has been proposed in Supplementary Note 1.

Liquid crystal interphase for MnO_2 deposition and beyond

Recognizing that ε-MnO_2 shares the same hexagonal crystal system as Zn, we aimed to implement the in situ liquid crystal phase strategy to the MnO_2 cathode in the DEFB. MnO_2 formed in the pristine electrolyte exhibits an uneven morphology with partly exposed graphite felt substrate (Supplementary Fig. 17). Conversely, the addition of surfactant facilitates a more uniform deposition, driven by favourable nucleation conditions (Supplementary Fig. 18). A high-resolution TEM image (Fig. 4a) reveals the (100) and (102) planes of ε-MnO_2, showing a tunnel structure[5] formed in the pristine electrolyte. Following surfactant incorporation, Fig. 4b highlights a noticeably increased lattice plane spacing of 0.72 nm, aligning well with the (002) planes of δ-MnO_2. XRD analysis using Mo radiation (Supplementary Fig. 19) corroborates the presence of ε-MnO_2 and δ-MnO_2 in the pristine electrolyte and surfactant electrolyte, respectively. Both share the hexagonal crystal system, but the δ-phase has a layered structure with a dominant (002) plane and enhanced electronic conductivity[11]. Hence, the introduction of surfactant results in a similar preferential orientation (*c* axis) in both Zn and MnO_2 and even causes MnO_2 to form as a different phase. The POM image with interference colour confirms the in situ formed liquid crystal interphase on MnO_2 (Fig. 4c), guiding the δ-phase growth. Further DFT calculations (Supplementary Figs. 20 and 21) elucidate the surfactant aggregation mechanisms on the δ-MnO_2 (002) plane and surfactant adsorption occurs via C–O bond formation. The possible phase change mechanism has been further discussed in Supplementary Note 2. Additionally, we noted restricted ZHS formation (Supplementary Figs. 22 and 23) and a reduction in defects concerning trivalent manganese (Supplementary Fig. 24), potentially due to the protective and coordinating[46] function of the liquid crystal interphase.

Beyond the hexagonal system, we conducted Cu deposition experiments, which are known to own the cubic crystal system to further investigate the influence of liquid crystal interphase on different crystal systems. Interestingly, Cu formed in the pristine electrolyte presents uneven and irregular octahedral morphology (Supplementary Fig. 25), whereas Cu formed in the surfactant electrolyte demonstrates a uniform cubic shape (Fig. 4d). Additional XRD assessments (Supplementary Fig. 26) indicate a prominent enhancement in the (200) plane of Cu developed in the surfactant electrolyte, suggesting a similar preferred *c*-axis orientation in the cubic system as well. Furthermore, this universal deposition strategy of texture control, mediated by liquid crystal phase, is independent of substrates, as evidenced by consistent deposition outcomes. Zn deposition on both titanium and graphite foils preserves the preferred (002) crystal plane orientation (Supplementary Fig. 27). This approach surpasses traditional substrate-controlled epitaxial growth[12,47], maintaining efficacy even at increasing distances from the substrate, as validated by grazing incidence XRD (GIXRD) analysis (Supplementary Fig. 28).

High-energy-density dual-electrode-free batteries

First, we aimed to identify the optimal surfactant additive concentration for the electrochemical performance of DEFBs (Cu foil||Carbon felt). Figure 4e demonstrates that a 0.1 mM surfactant concentration ensures the most extended cycling life (80% capacity retention for ~950 cycles) with a higher discharge capacity compared to the lower output and notable capacity decay of the pristine-electrolyte-based DEFB after ~250 cycles. Because the charging is at a fixed capacity, the CEs can be easily calculated. It can be observed that the cell with the

Fig. 4 | Liquid crystal interphase strategy for MnO_2 deposition and electrochemical performance of the DEFBs. a,**b**, TEM image of MnO_2 deposition using the pristine electrolyte (**a**) or surfactant electrolyte (**b**). Insets: schematics illustrating the crystal structure of ε-MnO_2 (**a**) and δ-MnO_2 (**b**) with the same hexagonal crystal system. Purple: manganese atom; red: oxygen atom. **c**, POM image of MnO_2 deposited on carbon fibre using the surfactant electrolyte. **d**, SEM image of Cu deposition on bare Cu with surfactant additive. Inset: schematic illustrating the cubic crystal system of Cu. **e**, Cycling tests using the electrolytes with different surfactant concentrations (charging at 2.3 V up to 0.5 mAh cm^{-2} and discharging at 5 mA cm^{-2} down to 1 V). Inset: the tenth cycle curve. **f**, Cycling tests using the pristine electrolyte or surfactant electrolyte (charging at 2.3 V up to 3 mAh cm^{-2} and discharging at 15 mA cm^{-2} down to 1 V). Inset: the tenth curve. **g**, Cycling tests using the pristine electrolyte or surfactant electrolyte (charging at 2.3 V up to 1 mAh cm^{-2} and discharging at 5 mA cm^{-2} down to 1 V) at −10 °C (top) and 60 °C (bottom). Insets: the tenth cycle curves. **h**, Cycling tests using the pristine electrolyte or surfactant electrolyte (charging at 2.3 V up to 1 mAh cm^{-2} and discharging at 5 mA cm^{-2} down to 1 V) without separator and sealing component under lean electrolyte amount (100 µl vs 1 ml). Inset: the tenth cycle curve. Refill: add water after capacity degradation.

https://doi.org/10.1038/s41560-024-01638-z

liquid crystal interphase (0.1 mM) maintains high CEs close to 100% for 200 cycles, whereas the maximum CE of the pristine one is less than 90%. The 1 mM concentration, however, hastens battery degradation, as indicated in POM images of the Zn surface (Supplementary Fig. 29). The images suggest that this concentration seems to foster a complete lamellar liquid crystal interphase, rather than the gradient interphase observed in the 0.1 mM surfactant electrolyte. Conversely, the 0.01 mM surfactant electrolyte falls short in forming liquid crystals.

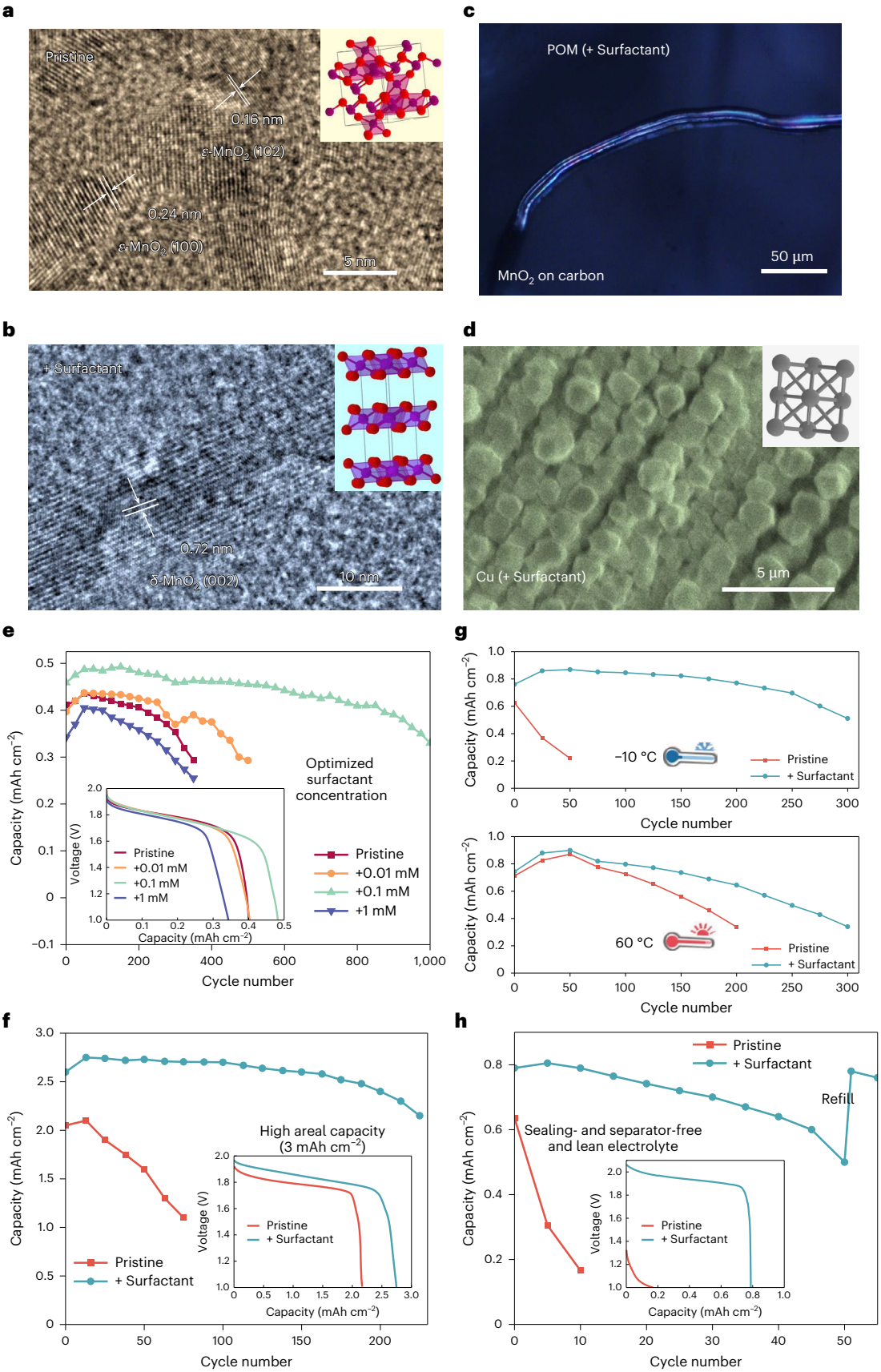

A thicker lamellar phase might hinder transport, contrasted by the potentially more dynamic-enhancing hexagonal phase with extensive 1-D channels[21]. In Supplementary Fig. 30, the liquid crystal interphase provides a high cation transference number (~0.72), facilitating the transport of cations while hindering anion movement. Further two-dimensional simulations indicate that liquid crystalline phases with anisotropic diffusion coefficients[48] can drastically reduce zinc dendrite growth by fostering better transport kinetics (Supplementary Fig. 31). The double-layer theory[49] and our findings suggest that the lamellar phase, functioning as a Helmholtz layer, may facilitate textured growth thermodynamically, whereas the hexagonal phase as a diffusion layer promotes uniform ion flux, enhancing kinetics. Therefore, achieving the appropriate gradient liquid crystal interphase structure (lamellar–hexagonal) is vital and the key lies in the concentration of surfactant in the electrolyte. For example, if the concentration is too high, liquid crystals may not be obtained, but rather possibly zinc oxide[50]. Besides, we found the chain length (n) of the surfactant (t-Oct-C_6H_4-$(OCH_2CH_2)_nOH$) plays a crucial role in determining the properties and behaviour of the liquid crystal interphase (Supplementary Fig. 32).

The 0.1 mM surfactant electrolyte is used for further electrochemical testing. Further analysis under more realistic conditions affirmed the liquid crystal interphase's positive impact on the practical application of DEFBs. Figure 4f sets a higher charging capacity (3 mAh cm^{-2}) for DEFBs, highlighting a widened cycle life gap between pristine electrolyte and surfactant electrolyte (50 vs 225 cycles). Concurrently, surfactant electrolyte yields higher voltage and capacity output with reduced polarization, attributed to minimized blockage from ZHS and augmented δ-MnO_2 conductivity under the liquid crystal interphase. This enhanced kinetic performance is more evident in the low-temperature test (Fig. 4g), where surfactant electrolyte maintains stable cycling at −10 °C, in remarkable contrast to the rapid degradation experienced by pristine electrolyte. Meanwhile, as shown in Supplementary Fig. 33, a potential advantage of this additive is that even short resting times can result in similar electrochemical performance. This may be due to the rapid self assembly of surfactant molecules and the lower viscosity of the electrolyte.

At higher temperatures, focusing on thermodynamic stability becomes pivotal. Utilizing surfactant electrolyte, which reduces the self-discharge rate (Supplementary Fig. 34), allows for longer cycling life at 60 °C (Fig. 4g), owing to greater corrosion resistance[51] and less hydrogen evolution reaction/oxygen evolution reaction activity. Applying separator-free[7] or sealing-free structures[52] (Supplementary Fig. 35) could further streamline components, maximizing battery energy density and cost effectiveness, albeit with a decreased cycle life due to the dissolution-shuttle effect of inactive Zn/MnO_2[53] and expedited water evaporation. Figure 4h presents a surfactant-electrolyte-based DEFB without separator and sealing components, sustaining ~50 cycles with a lean electrolyte volume (100 µl). This design allows capacity recovery through water refilling, mitigating capacity fading due to water evaporation. However, the pristine-electrolyte-based DEFB cannot regain capacity through refilling, as it lacks the liquid crystal interphase structure, resulting in a notable amount of irreversible deposition products associated with irreversible capacity loss. As estimated in Supplementary Table 1, this kind of component-free DEFB has an ultrahigh energy density of up to 213 Wh kg^{-1} based on the entire cell without external packaging, which is nearly six times that of traditional insertion-type Zn-MnO_2 batteries. Although its cycle life is shorter due to lower CE under extreme conditions, it is still a promising choice for high-energy-density aqueous batteries because it has the potential to break through grid applications and move towards scenarios such as electric vehicles. In fact, a shorter cycle life is a common issue for electrode-less batteries[9,10], and further optimization is expected in the future under extreme conditions such as lean electrolyte states.

Conclusions

In summary, as a conceptual work, we proposed the liquid crystal interphase chemistry and established a general strategy to regulate preferred deposition orientation for stable and high-energy-density aqueous batteries. In-depth soft matter characterizations reveal the in situ formation of a gradient liquid crystal interphase from a single surfactant molecular bilayer during charging. This surfactant-aggregation-induced interphase structure facilitates the templated growth of the hexagonal crystal system's (002) plane, enhancing deposition reversibility. Extending the long-established soft templating approach from colloid chemistry, we present a solution to the irreversible deposition issue in aqueous batteries. The full cells based on Zn/MnO_2 dual deposition with ultrahigh energy density exhibit notably enhanced cycling life using this local liquid crystal interphase, even under stringent and component-less conditions. The in situ formation of a liquid crystal interphase seems to be a more general phenomenon (Supplementary Fig. 36), potentially achievable with various surfactants under the right conditions, not limited to the specific surfactant initially reported in our study. We have outlined some potential key criteria for in situ generated liquid crystal phases as a reference (Supplementary Note 3). Furthermore, this facile approach may extend to other electrode systems such as cubic copper and even non-aqueous lithium (which needs to address SEI competitive growth), encouraging the customization of liquid crystal interphase structures to foster advancements in energy storage.

Methods

Materials preparation

$ZnSO_4·7H_2O$, $MnSO_4·H_2O$, $CuSO_4·5H_2O$, surfactants (t-Oct-C_6H_4-$(OCH_2CH_2)_nOH$, n = ~9–10/ ~ 5/ ~ 40), sodium dodecyl benzene sulfonate and glass fibre (Whatman GF/A and GF/D) were purchased from Sigma Aldrich. Zn foil, Cu foil, Ti foil, carbon foil and carbon felt were purchased from Thermo Fisher Scientific. The oxygen plasma treatment (SPI Supplies Plasma-Prep II system) activated the carbon felt before acting as a current collector. Deionized water was obtained from Milli-Q water purification system. 1 M $ZnSO_4$ and 1 M $MnSO_4$ were dissolved into the deionized water to prepare the pristine electrolyte, and the surfactant electrolyte was prepared by adding a surfactant with a concentration of 0.1 mM to pristine electrolyte for Zn/MnO_2 electrodeposition. 1 mM or 0.01 mM concentration of surfactant was also used for comparison. 1 M $CuSO_4$ and 1 M $MnSO_4$ were dissolved into the deionized water to prepare the electrolyte for Cu electrodeposition.

Electrochemical measurements

Zn/Cu half-cell tests were conducted in CR2032 coin cells on Land BT2000 battery test system with the areal capacity of 2 mAh cm^{-2} at the current density of 2 mA cm^{-2}. Cu foil was used for the current collector and the counter electrode is Zn foil. Glass fibre (GF/D) was used as separator and the electrolyte amount is 150 µl. In the initial-electrode-free batteries (DEFBs), Cu foil and carbon felt were used as the anode-free and cathode-free current collectors (1 cm^2), respectively, and pristine electrolyte or surfactant electrolyte was used as electrolyte, unless stated otherwise. One ml was the general used electrolyte whereas lean electrolyte amount is 100 µl. Glass fibre (GF/A) was used as separator unless the separator-free design. All DEFBs are housed in custom-made set-ups instead of traditional coin cell packaging, utilizing acrylic sheets and PTFE films as the outer layer to prevent corrosion. There is a small opening in the outer packaging of the battery to ensure the release of gas in the sealing-free design. Thin Cu foil and carbon coated Ti foil as terminal tabs for the anode and cathode current collectors were used to connect the test cables. For Zn/MnO_2 system, the DEFBs were charged at 2.3 V to a specific areal capacity, then discharged at constant current, and the cut-off voltage for discharge is 1 V. All the electrochemical experiments including electrochemical impedance spectroscopy (EIS) tests

were recorded by the VMP3 potentiostat (BioLogic). Besides room temperature, the DEFBs were also tested at −10 °C and 60 °C using an environmental chamber for controlled conditions.

Materials characterizations

The pH values were measured by a pH meter (METTLER TOLEDO). To investigate the deposition morphology and structure, we conducted a series of ex situ experiments. Electrodes were carefully extracted from the DEFBs at various charge/discharge states followed by a cleaning process with deionized water. SEM images were obtained with a Thermo Fisher Scientific Apreo S LoVac scanning electron microscope. Powder (regular) XRD and grazing incidence XRD were obtained with an Empyrean X-ray Diffractometer from PANalytical B.V. Pole figures were acquired from a PANalytical X'Pert 2. The above XRD results were based on Cu radiation whereas Mo radiation was selected as the high bright light source for Bruker Single Crystal D8 Venture for MnO_2 structural analysis. To identify the alignment of surfactant molecules before deposition, we immersed Cu foil in the specific solution (~600 s) and pulled it out as the model materials. Contact angles are characterized by a Rame–Hart 290 Goniometer to reflect the wettability. The chemical titration experiment on coated Cu was carried out by introducing an aqueous solution of 0.1 M KOH. Ellipsometry data were collected at Horiba UVISEL Ellipsometer, and we tested five points and got the average thickness. Note that coated Cu is required in a dry state and no salt is added to the electrolyte (only water and surfactant) to avoid additional signals from ellipsometry. The viscosity of the electrolytes was measured using the Rheosense 'Rheometer-on-a-chip' (model m-VROC-II). To confirm the formation of the liquid crystal interphase after deposition, the well-designed ex situ experiments were performed. The XPS characterization was performed on a PHI Versaprobe III with a monochromatized Al Kα X-ray source and Ar^+ etching (sputtering rate: ~1 nm min^{-1} for SiO_2). High-resolution spectra were calibrated using the C 1*s* peak at 284.8 eV. DLS tests were carried out using Brookhaven Instrument Nanobrook Omni particle size analyser with scattering angle of 90° and laser wavelength of 632.8 nm. One ml cuvettes were used in the DLS experiments, and to validate surfactant aggregation, thin zinc metal foil (0.1 mm) was trimmed and placed at the bottom of the cuvette before proceeding with DLS measurements. Only water and surfactant (0.1 mM) were used as the electrolyte for DLS tests. POM images were captured using Nikon's LV100 POL microscope with EPI Illuminator and colour camera head. To better protect the water-soluble liquid crystal phase on the surface from being destroyed by the cleaning process, a thin electrolyte film (approximately 1% of total electrolyte amount) is retained for further POM observation after the electrodes are disassembled from the DEFBs. Cryo-TEM analyses were conducted using a Thermofisher Titan 80–300 environmental transmission electron microscope. During the set-up, Cu TEM grids (Quantifoil R2/2) functioned as anode-free current collectors for Zn metal plating within the DEFBs, achieving a total capacity of 0.1 mAh cm^{-2} at a constant voltage of 2.3 V. The sample, prepared under liquid nitrogen, was secured in the Gatan side-entry cryo-transfer holder (model 626) to prevent air exposure and ice condensation, maintaining a temperature around −178 °C within the TEM column.

Surface energetics calculations

The DFT calculations were performed with the Vienna Ab-initio Simulation Package[54] using projector-augmented wave pseudopotentials[55], a plane wave basis set with a cut-off of 500 eV and a gamma-centred Monkhorst–Pack grid[56] (k points in each direction chosen by: 20 Å per (unit cell length)). All calculations were done at a generalized gradient approximation (GGA) level using the PBE functional. A convergence threshold of 10^{-5} eV was used for energies, whereas forces were converged to 0.02 eV $Å^{-1}$. A Hubbard U value of $U = 2.75$ was applied to the Mn 3*d* electrons[57].

Electrodeposition simulations

The two-dimensional computation about linear stability analysis[58,59] was performed by applying a small perturbation, $\varepsilon \exp(wt + iky)$, to a steady-state base state. In this perturbation, ε is the dimensionless small parameter, $i^2 = -1$, w is the growth rate (1 s^{-1}), k is the wavenumber (1 m^{-1}) that indicates the Zn metal surface roughness and ω is the molar volume of Zn metal (m^3 mol^{-1}). Electrodeposition is unstable if the perturbations grow with time, that is, if $w > 0$. The goal of a stability analysis is to express w in terms of physical properties, that is, diffusion coefficients, of the electrolyte.

Data availability

The data that support the findings of this study are available within this article and its Supplementary Information.

References

1. Li, W., Dahn, J. R. & Wainwright, D. S. Rechargeable lithium batteries with aqueous electrolytes. *Science* **264**, 1115–1118 (1994).
2. Liang, Y. & Yao, Y. Designing modern aqueous batteries. *Nat. Rev. Mater.* **8**, 109–122 (2023).
3. Parker, J. F. et al. Rechargeable nickel–3D zinc batteries: an energy-dense, safer alternative to lithium-ion. *Science* **356**, 415–418 (2017).
4. Chen, W. et al. A manganese–hydrogen battery with potential for grid-scale energy storage. *Nat. Energy* **3**, 428–435 (2018).
5. Zhong, C. et al. Decoupling electrolytes towards stable and high-energy rechargeable aqueous zinc–manganese dioxide batteries. *Nat. Energy* **5**, 440–449 (2020).
6. Chao, D. et al. An electrolytic Zn–MnO_2 battery for high-voltage and scalable energy storage. *Angew. Chem.* **131**, 7905–7910 (2019).
7. Li, G. et al. Membrane-free Zn/MnO_2 flow battery for large-scale energy storage. *Adv. Energy Mater.* **10**, 1902085 (2020).
8. Ming, F. et al. Co-solvent electrolyte engineering for stable anode-free zinc metal batteries. *JACS* **144**, 7160–7170 (2022).
9. Louli, A. J. et al. Diagnosing and correcting anode-free cell failure via electrolyte and morphological analysis. *Nat. Energy* **5**, 693–702 (2020).
10. Li, Y. et al. Interfacial engineering to achieve an energy density of over 200 Wh kg^{-1} in sodium batteries. *Nat. Energy* **7**, 511–519 (2022).
11. Xiao, X. et al. Ultrahigh-loading manganese-based electrode for aqueous battery via polymorph tuning. *Adv. Mater.* **35**, 2211555 (2023).
12. Zheng, J. et al. Reversible epitaxial electrodeposition of metals in battery anodes. *Science* **366**, 645–648 (2019).
13. Pileni, M.-P. The role of soft colloidal templates in controlling the size and shape of inorganic nanocrystals. *Nat. Mater.* **2**, 145–150 (2003).
14. Xiao, J. & Qi, L. Surfactant-assisted, shape-controlled synthesis of gold nanocrystals. *Nanoscale* **3**, 1383–1396 (2011).
15. Tiddy, G. J. Surfactant-water liquid crystal phases. *Phys. Rep.* **57**, 1–46 (1980).
16. Wang, D. et al. Insight on organic molecules in aqueous Zn-ion batteries with an emphasis on the Zn anode regulation. *Adv. Energy Mater.* **12**, 2102707 (2022).
17. Guan, K. et al. Anti-corrosion for reversible zinc anode via a hydrophobic interface in aqueous zinc batteries. *Adv. Energy Mater.* **12**, 2103557 (2022).
18. Bayaguud, A., Luo, X., Fu, Y. & Zhu, C. Cationic surfactant-type electrolyte additive enables three-dimensional dendrite-free zinc anode for stable zinc-ion batteries. *ACS Energy Lett.* **5**, 3012–3020 (2020).
19. Zhao, F. et al. Trace amounts of fluorinated surfactant additives enable high performance zinc-ion batteries. *Energy Storage Mater.* **53**, 638–645 (2022).

20. Lin, Y. et al. Dendrite-free Zn anode enabled by anionic surfactant-induced horizontal growth for highly-stable aqueous Zn-ion pouch cells. *Energy Environ. Sci.* **16**, 687–697 (2023).
21. Kato, T. et al. Transport of ions and electrons in nanostructured liquid crystals. *Nat. Rev. Mater.* **2**, 17001 (2017).
22. Li, Y., Yu, Z., Huang, J., Wang, Y. & Xia, Y. Constructing solid electrolyte interphase for aqueous zinc batteries. *Angew. Chem. Int. Ed.* **62**, e202309957 (2023).
23. Zeng, X. et al. Toward a reversible Mn^{4+}/Mn^{2+} redox reaction and dendrite-free Zn anode in near-neutral aqueous Zn/MnO_2 batteries via salt anion chemistry. *Adv. Energy Mater.* **10**, 1904163 (2020).
24. Yang, H. et al. Protocol in evaluating capacity of Zn–Mn aqueous batteries: a clue of pH. *Adv. Mater.* **35**, 2300053 (2023).
25. Chen, H. et al. Reunderstanding the reaction mechanism of aqueous Zn–Mn batteries with sulfate electrolytes: role of the zinc sulfate hydroxide. *Adv. Mater.* **34**, 2109092 (2022).
26. Yu, X. et al. Ten concerns of Zn metal anode for rechargeable aqueous zinc batteries. *Joule* **7**, 1145–1175 (2023).
27. Shi, F. et al. Strong texturing of lithium metal in batteries. *Proc. Natl Acad. Sci. USA* **114**, 12138–12143 (2017).
28. Yuan, D. et al. Anion texturing towards dendrite-free Zn anode for aqueous rechargeable batteries. *Angew. Chem.* **133**, 7289–7295 (2021).
29. Tiberg, F., Brinck, J. & Grant, L. Adsorption and surface-induced self-assembly of surfactants at the solid–aqueous interface. *Curr. Opin. Colloid Interface Sci.* **4**, 411–419 (1999).
30. Wang, N. et al. Zincophobic electrolyte achieves highly reversible zinc-ion batteries. *Adv. Funct. Mater.* **33**, 2300795 (2023).
31. Jin, S. et al. Production of fast-charge Zn-based aqueous batteries via interfacial adsorption of ion-oligomer complexes. *Nat. Commun.* **13**, 2283 (2022).
32. Thieghi, L. T., Longo, L. S. Jr, Licence, P. & Alves, S. Effect of dicationic ionic liquids on lyotropic liquid crystals formed by a binary system composed of Triton-X 100 and water. *Mol. Cryst. Liq. Cryst.* **657**, 95–101 (2017).
33. Deng, Y. et al. Nanomicellar electrolyte to control release ions and reconstruct hydrogen bonding network for ultrastable high-energy-density Zn–Mn battery. *JACS* **145**, 20109–20120 (2023).
34. Zhang, Z. et al. Capturing the swelling of solid-electrolyte interphase in lithium metal batteries. *Science* **375**, 66–70 (2022).
35. Cui, X., Mao, S., Liu, M., Yuan, H. & Du, Y. Mechanism of surfactant micelle formation. *Langmuir* **24**, 10771–10775 (2008).
36. Wang, Y. et al. Sulfolane-containing aqueous electrolyte solutions for producing efficient ampere-hour-level zinc metal battery pouch cells. *Nat. Commun.* **14**, 1828 (2023).
37. Sutherland, E., Mercer, S. M., Everist, M. & Leaist, D. G. Diffusion in solutions of micelles. What does dynamic light scattering measure? *J. Chem. Eng. Data* **54**, 272–278 (2009).
38. Ahir, S., Petrov, P. & Terentjev, E. Rheology at the phase transition boundary: 2. hexagonal phase of Triton X100 surfactant solution. *Langmuir* **18**, 9140–9148 (2002).
39. Wang, X. et al. Characterization of lipid-based lyotropic liquid crystal and effects of guest molecules on its microstructure: a systematic review. *AAPS PharmSciTech* **19**, 2023–2040 (2018).
40. Weiss, V., Thiruvengadathan, R. & Regev, O. Preparation and characterization of a carbon nanotube–lyotropic liquid crystal composite. *Langmuir* **22**, 854–856 (2006).
41. Oyafuso, M. H. et al. Development and in vitro evaluation of lyotropic liquid crystals for the controlled release of dexamethasone. *Polymers* **9**, 330 (2017).
42. Carey, C. R. et al. Imaging and absolute extinction cross-section measurements of nanorods and nanowires through polarization modulation microscopy. *J. Phys. Chem. C.* **114**, 16029–16036 (2010).
43. Yoshio, M., Mukai, T., Ohno, H. & Kato, T. One-dimensional ion transport in self-organized columnar ionic liquids. *JACS* **126**, 994–995 (2004).
44. Lin, Z. et al. Scalable solution-phase epitaxial growth of symmetry-mismatched heterostructures on two-dimensional crystal soft template. *Sci. Adv.* **2**, e1600993 (2016).
45. Kum, H. et al. Epitaxial growth and layer-transfer techniques for heterogeneous integration of materials for electronic and photonic devices. *Nat. Electron.* **2**, 439–450 (2019).
46. Hong, S. et al. Efficient scalable hydrothermal synthesis of MnO_2 with controlled polymorphs and morphologies for enhanced battery cathodes. *ACS Energy Lett.* **8**, 1744–1751 (2023).
47. Hao, Z. et al. Metal anodes with ultrahigh reversibility enabled by the closest packing crystallography for sustainable batteries. *Adv. Mater.* **35**, 2209985 (2023).
48. Chen, C.-H., Postlethwaite, T. A., Hutchison, J. E., Samulski, E. T. & Murray, R. W. Electrochemical measurements of anisotropic diffusion in thin lyotropic liquid crystal films using interdigitated array electrodes. *J. Phys. Chem.* **99**, 8804–8811 (1995).
49. Sun, W. et al. A rechargeable zinc-air battery based on zinc peroxide chemistry. *Science* **371**, 46–51 (2021).
50. Zhang, Y. et al. Nonionic surfactant-assisted in situ generation of stable passivation protective layer for highly stable aqueous Zn metal anodes. *Nano Lett.* **22**, 8574–8583 (2022).
51. Ghavami, R. K. & Rafiei, Z. Performance improvements of alkaline batteries by studying the effects of different kinds of surfactant and different derivatives of benzene on the electrochemical properties of electrolytic zinc. *J. Power Sources* **162**, 893–899 (2006).
52. Wang, F. et al. Production of gas-releasing electrolyte-replenishing Ah-scale zinc metal pouch cells with aqueous gel electrolyte. *Nat. Commun.* **14**, 4211 (2023).
53. Ye, X. et al. Unraveling the deposition/dissolution chemistry of MnO_2 for high-energy aqueous batteries. *Energy Environ. Sci.* **16**, 1016–1023 (2023).
54. Kresse, G. & Furthmüller, J. Efficient iterative schemes for ab initio total-energy calculations using a plane-wave basis set. *Phys. Rev. B* **54**, 11169–11186 (1996).
55. Kresse, G. & Joubert, D. From ultrasoft pseudopotentials to the projector augmented-wave method. *Phys. Rev. B* **59**, 1758–1775 (1999).
56. Monkhorst, H. J. & Pack, J. D. Special points for Brillouin-zone integrations. *Phys. Rev. B* **13**, 5188–5192 (1976).
57. Carlson, E. Z., Chueh, W. C., Mefford, J. T. & Bajdich, M. Selectivity of electrochemical ion insertion into manganese dioxide polymorphs. *ACS Appl. Mater. Interfaces* **15**, 1513–1524 (2023).
58. Li, W., Tchelepi, H. A., Ju, Y. & Tartakovsky, D. M. Stability-guided strategies to mitigate dendritic growth in lithium-metal batteries. *J. Electrochem. Soc.* **169**, 060536 (2022).
59. Li, W., Tchelepi, H. A. & Tartakovsky, D. M. Screening of electrolyte-anode buffers to suppress lithium dendrite growth in all-solid-state batteries. *J. Electrochem. Soc.* **170**, 050510 (2023).

Acknowledgements

This work is supported by the Aqueous Battery Consortium, an energy innovation hub under the US Department of Energy, Office of Basic Energy Sciences, Division of Materials Science and Engineering. We also acknowledge the use and support of the Stanford Nano Shared Facilities and the Stanford Nanofabrication Facility and the use of the computer time allocation m2997 at the National Energy Research Scientific Computing Center, a DOE Office of Science User Facility supported by the Office of Science of the US Department of Energy under contract number DE-AC02-05CH11231. Y.C. acknowledges cryo-EM support from the US Department of Energy, Office of Basic Energy Sciences, Division of Materials Science and Engineering under

contract DE-AC02-76SF00515. M.B. acknowledges support by the US Department of Energy, Office of Science, Office of Basic Energy Sciences, Chemical Sciences, Geosciences and Biosciences Division, Catalysis Science Program, to the SUNCAT Center for Interface Science and Catalysis.

Author contributions

Y.L. and Y.C. (corresponding author) conceived the project and designed the experiments. Y.L. performed electrochemical measurements and soft matter characterizations. Y.L. and X.X. performed SEM and XRD experiments. E.Z.C. and M.B. carried out DFT calculations. W.L. carried out two-dimensional computation. Y.C. carried out cryo-(S)TEM experiments. Y.Y. performed XPS experiments. All authors discussed the results and commented on the manuscript.

Competing interests

The authors declare no competing interests.

Additional information

Supplementary information The online version contains supplementary material available at https://doi.org/10.1038/s41560-024-01638-z.

Correspondence and requests for materials should be addressed to Yi Cui.

Peer review information *Nature Energy* thanks Yi-Chun Lu and the other, anonymous, reviewer(s) for their contribution to the peer review of this work.

Reprints and permissions information is available at www.nature.com/reprints.

Publisher's note Springer Nature remains neutral with regard to jurisdictional claims in published maps and institutional affiliations.

Springer Nature or its licensor (e.g. a society or other partner) holds exclusive rights to this article under a publishing agreement with the author(s) or other rightsholder(s); author self-archiving of the accepted manuscript version of this article is solely governed by the terms of such publishing agreement and applicable law.

© The Author(s), under exclusive licence to Springer Nature Limited 2024